

1 New mechanism of fibronectin fibril assembly revealed by live imaging and super-resolution
2 microscopy.

3
4 Darshika Tomer¹, Sudipto Munshi², Brianna E. Alexander^{1,3}, Brenda French², Pavan Vedula⁴,
5 Andrew House⁵, Murat Guvendiren⁵, Anna Kashina⁴, Jean E. Schwarzbauer⁶, and Sophie
6 Astrof^{1,*}.

- 7
8 1. Department of Cell Biology and Molecular Medicine, Cardiovascular Research Institute,
9 Rutgers Biomedical and Health Sciences, 185 South Orange Ave, Newark, NJ, 07103,
10 USA.
11
12 2. Sidney Kimmel Medical College of Thomas Jefferson University, Philadelphia, PA,
13 19107, USA
14
15 3. Multidisciplinary PhD Program in Biomedical Sciences. Cell Biology, Neuroscience and
16 Physiology track, Rutgers Biomedical and Health Sciences, Newark, NJ, 07103, USA.
17
18 4. Department of Biomedical Sciences, University of Pennsylvania, Philadelphia, PA
19 19104, USA
20
21 5. Otto H. York Chemical and Materials Engineering, Department of Biomedical
22 Engineering, New Jersey Institute of Technology, Newark, NJ 07102, USA
23
24 6. Department of Molecular Biology, Princeton University, Princeton, New Jersey, USA
25
26

27 *Author for correspondence: Sophie Astrof, Ph.D.

28 Phone: 617-429-8295

29 E-mail: sophie.astrof@rutgers.edu

30 **Abstract**

31• The regulation of cell fate decisions, morphogenesis, and responses to injury are intimately
32 linked to the process of Fn1 fibrillogenesis. Live imaging and super-resolution microscopy
33 revealed that Fn1 fibrils are not continuous. Instead, Fn1 fibrils arise from nanodomains
34 containing multiple Fn1 dimers. As they move toward cell center, Fn1 nanodomains become
35 organized into linear arrays with a spacing of 130 nm between the nanodomains, with little Fn1
36 in between; Fn1 nanodomain arrays are resistant to deoxycholate treatment demonstrating
37 that these beaded assemblies are indeed mature Fn1 fibrils. FUD, a bacterial peptide that
38 disrupts Fn1 fibrillogenesis, does not disrupt nanodomain formation; instead, it interferes with
39 the organization of nanodomains into arrays. The nanodomain composition of Fn1 fibrils is
40 observed in multiple contexts: in three-dimensional ECM *in vivo*, on substrata of different
41 composition and stiffness, and is retained in the absence of cells. The modular architecture of
42 Fn1 fibrils bears important implications for mechanisms of ECM remodeling and signal
43 transduction.

44 **Introduction**

45 Fibronectin (Fn1) is a requisite component of extracellular matrix (ECM) necessary for
46 embryogenesis and homeostasis (1). It is noteworthy that in the absence of Fn1 fibrillogenesis,
47 the binding of Fn1 to cells is not sufficient to regulate key biological processes including those
48 governing embryonic development, angiogenesis, vascular remodeling, or cartilage
49 condensation (2-5). Therefore, understanding the mechanisms by which Fn1 proteins
50 assemble into macromolecular fibrils is essential to gain insights into *in vivo* functions of Fn1.
51 Fn1 fibrillogenesis occurs following the binding of secreted Fn1 homodimers to cell-surface
52 integrins. Following integrin binding, intracellular cytoskeletal forces such as actomyosin
53 contractility acting through integrins generate pulling forces on Fn1 dimers, exposing epitopes
54 that promote Fn1 fibrillogenesis (6-10). At the cell biological level, the process of Fn1
55 fibrillogenesis is correlated with the formation of fibrillar adhesions, whereby mobile adhesions
56 containing Fn1 and integrin $\alpha 5\beta 1$ translocate toward the nucleus resulting in elongated linear
57 arrays termed focal and fibrillar adhesions, containing both Fn1 and intracellular cytoplasmic
58 effectors linking Fn1 and actin cytoskeleton (11-16).

59 It has been thought that Fn1 fibrils arise following partial unfolding and alignment of Fn1
60 dimers in a periodic end-to-end fashion of alternating N- and C-termini, forming continuous
61 fibers (17-19). However, this model is based on the analyses of fixed samples and electron
62 microscopy wherein the exact composition of the fibrous material imaged could not be easily
63 determined. To evaluate the process of fibrillogenesis in real time, we adopted a
64 CRISPR/Cas9-mediated mutagenesis approach to generate fluorescently-labeled Fn1, subject
65 to physiological regulation of expression and splicing. This approach has enabled us to
66 visualize the initiation and progression of Fn1 fibrillogenesis over an extended period of time.
67 Using live imaging and super resolution microscopy, we uncovered an unexpected mechanism
68 of Fn1 fibrillogenesis. Our data demonstrate that Fn1 fibrils are composed of centripetally-

69 moving Fn1 nanodomains originating at cell periphery. As Fn1 nanodomains move toward the
70 nucleus, they become arranged into progressively longer and longer arrays wherein
71 nanodomains containing a high number of Fn1 dimers alternate with regions containing low or
72 no Fn1. We show that the N-terminal Fn1 assembly region is not required for the formation of
73 Fn1 nanodomains or their centripetal translocation. Instead, the N-terminus of Fn1 regulates
74 the organization of Fn1 nanodomains into linear arrays. This model of fibrillogenesis integrates
75 the process of fibrillogenesis with adhesion maturation and provides significant new insights
76 into the mechanisms of ECM formation, remodeling, and signaling.

77

78 **Results**

79 While examining Fn1⁺ ECM by confocal immunofluorescence microscopy in mouse
80 embryos, we observed that Fn1 fibrils appeared discontinuous (**Fig. 1A-B**, arrows), containing
81 regularly-spaced regions of high and low fluorescence intensity (**Fig. 1C, Movie 1**). This
82 suggested that Fn1 fibrils consisted of regions with a high number of Fn1 dimers separated by
83 regions containing a low number of Fn1 dimers (**Fig. 1C**). To test this hypothesis and to
84 determine mechanisms regulating the formation of Fn1 fibrils, we employed a CRISPR/Cas9
85 knock-in strategy to modify the endogenous Fn1 locus by replacing the termination codon of
86 Fn1 with a sequence encoding a fluorescent protein. This strategy has allowed to generate
87 fluorescently-labeled Fn1 proteins subject to endogenous regulation (**Sup. Fig. 1A-B**), and
88 enabled extended live imaging of Fn1 fibrillogenesis. Using this strategy, we obtained multiple
89 independent lines of mouse embryo fibroblasts (MEFs) expressing Fn1-mEGFP, Fn1-
90 mScarlet-I, Fn1-Neon Green, or Fn1-tdTomato fusion proteins (FP) generated by
91 CRISPR/Cas9-mediated insertion. Western blots showed that FP fusions to Fn1 were specific:
92 FPs were only fused to Fn1 as no other FP fusions were detected either by western blotting or
93 immunofluorescence (IF) (**Sup. Fig. 2A-B**).

94 Deoxycholate (DOC) insolubility of Fn1 ECM is a classical biochemical assay for
95 proteins stably incorporated into the assembled ECM (20-23). DOC assays demonstrated that
96 the incorporation of Fn1-FPs into ECM was indistinguishable from wild-type, untagged Fn1
97 (**Sup. Fig. 2C**). To determine whether Fn1-FP proteins carried out the physiological functions
98 of Fn1, we generated Fn1^{mEGFP} knock-in mice. Fn1^{mEGFP/mEGFP} homozygous knock-in animals
99 are viable and fertile (**Sup. Fig. 1B** panels 4 and 5). Furthermore, Fn1-mEGFP proteins were
100 expressed in the same pattern as total Fn1 protein (**Sup. Fig. 2d**) (24). Together, these studies
101 demonstrated that Fn1-FP fusion proteins are suitable reagents for investigating mechanisms
102 of Fn1 fibrillogenesis.

103 To visualize the process of fibrillogenesis in real time, we plated Fn1^{mEGFP/+} MEFs on
104 gelatin-coated cover glass and imaged cells 16 hours after plating using total internal reflection
105 (TIRF) microscopy at the critical angle of incidence. These experiments showed that Fn1
106 fibrillogenesis initiated at cell periphery as distinct bright Fn1 densities that moved centripetally
107 in parallel with F-actin and aligned into linear arrays of “beads” (arrows in **Movie 2**). TIRF
108 imaging also showed that the domains of higher fluorescence intensity of Fn1 co-localized with
109 integrin $\alpha 5\beta 1$ both in non-fibrillar adhesions (arrows in **Fig. 2A-A2**) and in fibrillar adhesions
110 (arrows in **Fig. 2B-B2**), and that Fn1 and $\alpha 5\beta 1$ fibrillar adhesions are beaded (**Fig. 2B-B2**,
111 arrows). We also observed the beaded architecture of Fn1 fibrils using an independent
112 imaging method by employing Zeiss Airyscan (**Sup. Fig. 3**). Staining using monoclonal and
113 polyclonal antibodies recognizing distinct and multiple epitopes in Fn1 resulted in the
114 discontinuous appearance of Fn1 fibrils (**Fig. 3A1-C1**). Fn1 fibrils formed by cells plated on
115 glass, gelatin, laminin 111 or vitronectin were beaded Fn1 fibrils (**Fig. 3**, and **Sup. Figs. 3-4**),
116 and so were Fn1 fibrils in cell-free areas (**Fig. 3A, A1**) and between cells (**Fig. 3B-C**). In
117 addition, the beaded appearance of Fn1 fibrils was observed when cells were plated on soft
118 substrata such as hydrogels of variable stiffness (**Sup. Fig. 4C-D**). In the latter experiment,

119 Fn1 was detected by imaging the native fluorescence of Fn1-mEGFP, indicating that the
120 beaded appearance of Fn1 fibrils was independent of antibody staining. Taken together, these
121 studies indicated that the beaded appearance of Fn1 fibrils was a general feature of Fn1 ECM
122 seen in 3D ECM *in vivo* and under different conditions *in vitro*.

123 To test the hypothesis that the “beads” in Fn1 strings were contiguous, cultures were
124 treated with 2% DOC. 2% DOC treatment dissolves cell membranes and cytoplasmic
125 components, leaving insoluble ECM devoid of cell contact (see **Movie 3** for time-laps of
126 dissolution of cellular components, F-actin and DNA). This experiment showed that Fn1 fibrils
127 in assembled ECM retained their beaded architecture in the absence of cell contact (**Fig. 3D**).
128 Together, these data indicated that the beaded topology of Fn1 fibrils is a feature of
129 physiological three-dimensional Fn1 ECM *in vivo* and suggested that the beads are
130 contiguous.

131 To determine the relationship between the beaded architecture of Fn1 seen by
132 diffraction-limited microscopy with Fn1 nanoarchitecture, we plated Fn1^{mEGFP/+} MEFs on glass
133 for 16 hours, then fixed and stained cells using a monoclonal antibody to the central region of
134 Fn1. Fn1-mEGFP fluorescence was imaged in the TIRF mode at the critical angle of incidence,
135 while the binding of the monoclonal α Fn1 antibody was detected with Alexa Fluor-647-
136 conjugated secondary antibody and imaged by Stochastic Optical Reconstruction Microscopy
137 (STORM). STORM was performed by illuminating samples at the critical angle of incidence, as
138 described in (25). Thin beaded fibrillar adhesions (arrow in **Fig. 4A**) were resolved by STORM
139 (**Fig. 4B-B2**) to be arrays of regularly-spaced nanodomains that were symmetrical in x, y, and
140 z dimensions (**Fig. 4B1, B2, B2'** and **Movie 4**). The space between nanodomains contained a
141 few or no Fn1 localizations (**Fig. 4B2** and **Movie 4**).

142 Fn1 is a large, multi-domain, ~250 kDa glycoprotein secreted as a homodimer, wherein
143 Fn1 subunits are linked in the anti-parallel orientation by two di-sulfide bonds at their C-termini

144 (1, 26). To investigate the relationship between the domain structure of Fn1 protein and the
145 nanodomain architecture of Fn1 fibrils, we used antibodies to distinct parts of Fn1 protein
146 (depicted in **Model 1** at the bottom of **Fig. 5**.) and STORM. For these experiments, wild-type
147 and Fn1^{mEGFP/+} MEFs were sparsely-plated in Ibidi 8-well glass-bottom chambers overnight,
148 allowing to observe the structure of thin fibrils. Cells were then fixed and stained with
149 antibodies recognizing different Fn1 epitopes: polyclonal rabbit antibodies raised to recognize
150 the first six type III repeats of Fn1 (Fn1 III₁₋₆) (27) (**Fig. 5** column 1), a monoclonal antibody
151 recognizing an epitope within the central region of Fn1 (**Fig. 5** columns 2, 4-5), polyclonal anti-
152 serum 297.1 raised against the entire Fn1 protein (28) (**Fig. 5**, column 3), or polyclonal
153 antibodies to GFP, recognizing the C-terminus of Fn1-mEGFP protein (**Fig. 6**, column 5). To
154 maximize the labeling density, the polyclonal anti-Fn1 III₁₋₆ and 297.1 antisera were used at a
155 40- and 4-fold higher concentrations than for routine immunofluorescence microscopy,
156 respectively. Together with the use of excess secondary antibodies each conjugated to 3 – 6
157 molecules of Alexa-647, this approach maximizes the chance that all the epitopes recognized
158 by the 1^o antibodies will be localized by STORM (25).

159 We first focused on the analyses of thin Fn1 fibrils like those marked by the arrows in
160 (**Fig. 4A-B**) to study the initiation of fibril formation rather than fibril bundling or branching.
161 Each antibody resulted in the detection of long characteristic Fn1 fibrils (**Fig. 5A-C**).
162 Successive magnifications show that independent of the antibody used for staining, Fn1 fibrils
163 contained linear arrays of nanodomains (thin arrows in **Fig. 5D**, **magnified in 5E**) separated
164 by regions containing a small number or no Fn1 localizations (as in **Fig. 4**, **Movie 4**).

165
166 Surprisingly, staining with the polyclonal anti-serum 297.1 raised to the entire Fn1 and,
167 presumably, recognizing multiple epitopes along Fn1, resulted in the same pattern of regularly-
168 spaced nanodomains as staining with antibodies recognizing distinct parts of Fn1 molecule

169 (**Fig. 5**, column 3), suggesting that each Fn1 localization contained the entire Fn1 sequence,
170 and that each nanodomain contained multiple Fn1 dimers.

171

172 These data are not consistent with previous models suggesting that Fn1 fibrils are composed
173 of periodically aligned Fn1 dimers arranged in an end-to-end fashion of alternating N- and C-
174 termini (17-19) (**Model 1** at the bottom of **Fig. 5**). Such periodic alignment of Fn1 dimers
175 necessitates that staining using polyclonal antibodies would result in a uniform labeling of thin
176 Fn1 fibrils, as depicted in **Model 1**. The dimers in the **Model 1** are aligned in an end-to-end
177 fashion, according to the current Fn1 fibrillogenesis model, with the predicted overlap between
178 the N-terminal Fn1 assembly domain (blue) and the first six type III repeats of Fn1 (red) (21)).
179 If Fn1 fibrils, were indeed composed of continuous, linear arrays of dimers, the use of all four
180 depicted in **Model 1** would be predicted to uniformly label Fn1 fibrils.

181

182 To test this prediction, we used Fn1^{mEGFP/+} MEFs and a cocktail of four antibodies recognizing
183 the beginning (α Fn1 III₁₋₆), middle- (α Fn1 monoclonal), and the end (α GFP) of Fn1-mEGFP
184 protein in addition to all the epitopes recognized by 297.1 polyclonal antibody. The binding of
185 all the antibodies in the cocktail was detected by a cocktail of secondary antibodies that were
186 each conjugated to 3 – 6 molecules of Alexa-647 (**Fig. 5**, column 7). The nanoarchitecture of
187 thin Fn1 fibrils, the nanodomain spacing (124 ± 25 nm between nanodomains in fibrils, on
188 average), nanodomain size (average diameter 77 ± 18 nm), and the number of Fn1
189 localizations per nanodomain (average of 80 ± 43 localizations) detected by the cocktail of four
190 antibodies were indistinguishable from those produced by each type of the antibody
191 individually (**Fig. 5D – E**, quantified in **Fig. 5F-H** and **Tables 1 –3**). These results indicate that
192 Fn1 fibrils are not uniform. Instead, our data show that Fn1 fibrils are arrays of nanodomains
193 containing multiple Fn1 dimers separated by areas containing a few or no Fn1 molecules (**Fig.**

194 **5, Model 2**). The nanoarchitecture of Fn1 fibrils following the treatment with 2% DOC which
195 removes cells and cellular components, was similar to untreated fibrils (**Fig. 5**, columns 4 and
196 **8, Fig. 5F – H**). These data indicate that the nanodomain architecture is a feature of mature
197 Fn1 fibrils.

198
199 Fn1 nanodomains were also present outside of fibrils, we term them non-fibrillar nanodomains
200 (e.g. notched arrowheads in **Fig. 4**). About 3 – 5 such nanodomains are seen as a “bead” in
201 conventional diffraction-limited microscopy. Non-fibrillar Fn1 nanodomains contained a similar
202 number of Fn1 localizations per nanodomain and were of similar size compared with Fn1
203 nanodomains in fibrils (**Fig. 5H, Tables 2 – 3**). Staining using antibodies to endosomal and
204 lysosomal markers (Rab5 and LAMP1) showed no appreciable co-localization with Fn1
205 nanodomains (data not shown). Together with imaging using TIRF microscopy, these findings
206 indicated that Fn1 nanodomains in fibrils and non-fibrillar nanodomains are on the cell surface.
207 Non-fibrillar Fn1 nanodomains were present at cell periphery and throughout the cell surface,
208 but they were not organized into linear arrays and were spaced at an median distance of 329
209 nm (**Table 1**).

210 Live imaging experiments suggested that Fn1 fibrils form from centripetally-translocating
211 Fn1 nanodomains originating at cell periphery (**Movie 2**). To understand the relationship
212 between the observed nanodomain architecture of Fn1 fibrils and the process of fibrillogenesis,
213 we adopted a live imaging approach using Fn1^{mEGFP/+} MEFs and inhibitors of fibrillogenesis.
214 Fn1 fibrillogenesis critically depends on the interactions mediated by the N-terminal assembly
215 domain of Fn1 (domains shaded in blue in **Model 1, Fig. 5**), and inhibitors that interfere with
216 these interactions block the formation of Fn1 fibrils (29-34). One such inhibitor is a 49-amino
217 acid peptide derived from *Streptococcus pyogenes* adhesin F1, termed the functional
218 upstream domain (FUD) (31). FUD binds the N-terminal assembly domain of Fn1 and
219 functions as a competitive inhibitor of Fn1-Fn1 interactions (31, 35). To determine how N-

220 terminal interactions regulate Fn1 fibrillogenesis, Fn1^{mEGFP/+} MEFs were plated on glass for 4
221 hours, and then imaged for 15 – 18 hours either in the imaging medium alone, or in the
222 medium containing either 225 nM FUD or 274 nM 11-IIIC, a 68 amino-acid control peptide that
223 does not interfere with Fn1 fibrillogenesis (32, 36). Untreated cells or cells treated with the
224 control peptide developed and accumulated long Fn1 fibrils (**Movie 5**). In contrast, treatment
225 with FUD led to dismantling of the pre-existing Fn1 fibrils and inhibited the formation of new
226 Fn1 fibrils (**Movie 6**). Instead of fibrils, cells cultured in the presence of FUD mainly contained
227 centripetally-moving Fn1-mEGFP fluorescent “beads” that only rarely formed strings (**Movie 6**).
228 These experiments suggested that FUD inhibits fibrillogenesis by interfering with the process
229 by which Fn1 “beads” become arranged or connected into linear arrays. To test this
230 hypothesis, Fn1^{mEGFP/+} MEFs were plated for 16 hours in the continuous presence of either
231 225 nM FUD or 274 nM III-11C control peptides, or were left untreated. Cell were then fixed
232 and stained without permeabilization using monoclonal anti-Fn1 antibodies which were
233 detected with Alexa Fluor 647-conjugated secondary antibodies, and imaged at the critical
234 angle of incidence by STORM at the excitation wavelength of 640 nm (25). This approach
235 abolishes the detection of intracellular Fn1-mEGFP and maximizes the detection of cell-
236 surface Fn1 due to the following: a) the absence of a detergent during fixation, staining and
237 washing, b) detecting the emission of Alexa 647-conjugated antibodies at ≥ 670 nm, c) the use
238 of oxygen scavengers in the STORM buffer that inhibits GFP fluorescence (37), and d)
239 imaging at the critical angle of incidence to detect fluorescence in close proximity to the
240 plasma membrane. These experiments demonstrated that the organization of nanodomains
241 into linear arrays was lost upon incubation with FUD (compare **Fig. 6A, B, A1, B1** with **Fig.**
242 **6C, C1**). Non-fibrillar Fn1 nanodomains in cells treated with FUD had a similar number of Fn1
243 localizations per nanodomain, and were of similar sizes compared with fibrillar or non-fibrillar
244 Fn1 nanodomains in untreated cells or cells incubated with the control peptide (**Fig. 6A2, 6B2,**
245 **and 6C1-1**, quantified in Fig. **6D** and **Tables 2-3**). Taken together, these data indicate that

246 FUD does not interfere with the formation of Fn1 nanodomains but inhibits the organization of
247 Fn1 nanodomains into linear arrays. Since Fn1 proteins lacking the N-terminal assembly
248 domain do not form fibrils, our experiments suggest that interactions mediated by the N-
249 terminal assembly domain of Fn1 are critical for the linking of Fn1 nanodomains into strings.

250

251 **Discussion**

252 In this manuscript, we describe the discovery of a novel mechanism underlying the process of
253 Fn1 fibrillogenesis. We found that the three-dimensional beaded architecture of Fn1 ECM
254 fibrils *in vivo* and in two-dimensional cell culture is due to the presence of Fn1 nanodomains,
255 and showed that each Fn1 nanodomain is composed of multiple Fn1 dimers. Time-laps
256 imaging by confocal and TIRF microscopy showed that Fn1 fibrillogenesis initiated at cell
257 periphery, as bright fluorescent “beads” of Fn1-mEGFP moved centripetally in parallel with F-
258 actin and became organized into linear arrays. Interestingly, the beaded appearance of focal
259 and fibrillar adhesions has been noted before (13, 16), and the beaded architecture of cell
260 adhesions can be seen in micrographs from multiple studies (e.g. Fig. 1C in (16), Fig 7a and
261 Sup. Figs 1a and b in (38); Fig. 8B in (39); and lower left cell in Fig. 3A (40). However, the
262 significance of these observations has not been investigated to the best of our knowledge. Fn1
263 domains and beaded strings in our movies resemble mobile, Fn1⁺ adhesions similar to those
264 described previously (13-16). The centripetal movement of these adhesions was dependent on
265 the rearward actin flow, and the linkage of Fn1 to actin was mediated by integrin $\alpha 5\beta 1$ and
266 tensin (13, 15, 16). Our TIRF microscopy experiments are consistent with these studies and
267 show that integrin $\alpha 5\beta 1$ co-localizes with the regions of higher Fn1 intensity in fibrillar and non-
268 fibrillar adhesions, and that $\alpha 5\beta 1^+$ focal and fibrillar adhesions are beaded. Taken together, our
269 studies suggest that Fn1 fibrils arise from small mobile nanodomains containing Fn1⁺ and
270 integrin $\alpha 5\beta 1^+$ that move toward the cell’s center. This centripetal translocation of Fn1

271 nanodomains is coordinated with their organization into linear arrays, which become longer
272 and longer as more nanodomains are added.

273

274 The number of Fn1 localizations in nanodomains is independent of the antibody type or
275 amount used for staining, indicating that we are using saturating amounts of antibodies.

276 Together with the preservation of the nanodomain architecture upon the treatment with DOC,
277 our studies indicate that the non-uniform, beaded architecture is a salient feature of mature
278 Fn1 fibrils. Two pieces of evidence suggest that Fn1 nanodomains in fibrils are contiguous: 1)
279 the preservation of the linear organization and the nanoarchitecture of Fn1 fibrils after the
280 treatment of cells with DOC which dissolves cell membranes, and 2) the presence of fibrous
281 material between immunogold densities in electron micrographs (18, 19, 41). The sparsity of
282 Fn1 localizations between Fn1 nanodomains in fibrils indicates that molecules other than or in
283 addition to Fn1 participate in the linking of Fn1 nanodomains into strings.

284

285 FUD peptide specifically binds to the N-terminal assembly domain of Fn1 (35, 42) and acts as
286 a competitive inhibitor of Fn1-Fn1 interactions (31, 43). In the absence of FUD, individual fibrils
287 in an established matrix are stable and can be tracked for over 16 hours (data not shown).

288 When FUD is added to cells, it specifically co-localizes with Fn1 fibrils and dismantles the
289 mature Fn1 ECM (31, 34), suggesting that the linear arrangement of Fn1 nanodomains in the
290 fibrillar ECM is maintained through dynamic interactions mediated at least in part by the Fn1 N-
291 terminal assembly domain. Our live imaging experiments demonstrated that in addition to
292 dismantling pre-existing fibrils, FUD effectively blocks their de-novo formation. STORM
293 showed that FUD does not affect the formation of Fn1 nanodomains, instead, it blocks the
294 organization of Fn1 nanodomains into linear arrays. Together, these data suggest that FUD
295 may block the dynamic interactions between the N-terminal Fn1 assembly domain and the
296 factor(s) linking Fn1 nanodomains into fibrils.

297

298 The beaded architecture of Fn1 ECM has important implications for the mechanisms of ECM
299 formation, remodeling and signal transduction. The tensile strength of knotted strings is
300 significantly lower than that of strings with uniformly-aligned fibers (44, 45), thus the beaded
301 architecture of Fn1 fibrils may facilitate their rupture under strain (46). The non-uniform,
302 nanodomain architecture of Fn1 may facilitate the accessibility of Fn1 fibrils to matrix
303 metalloproteases. In this model, degradation of Fn1 fibrils by metalloproteases may be
304 accomplished by cleaving between Fn1 nanodomains facilitating ECM remodeling. Finally, Fn1
305 is known to bind growth factors (47-49), and cell adhesion to ECM is known to orchestrate
306 growth factor signaling (50). Thus, Fn1 nanodomains could serve as platforms for the binding
307 and presentation of concentrated packets of growth factors to cells, the organization of Fn1
308 nanodomains into closely-spaced arrays could further facilitate clustering and signaling by
309 growth factor receptors.

310

311 **Acknowledgements**

312 We thank Richard Hynes and Nathan Astrof for insightful discussions and careful reading of
313 the manuscript, Sydney Astrof for help with data entry and encouragement, Patrick Murphy for
314 endothelial cells, Richard Hynes for the gift of 297.1 antibody, and Tung Chan for help with
315 setting up Western Blotting using ProteinSimple.

316

317 **Sources of Funding** This work was supported by the funding from the National Heart, Lung,
318 and Blood Institute of the NIH R01 HL103920 and R01 HL134935 to SA, by the NIH Office of
319 the Director R21 OD025323-01 to SA, by the pre-doctoral fellowship F31HL151046 to BEA, by
320 the National Institute of General Medicine R35GM122505 to AK, by the National Institute of
321 Arthritis and Musculoskeletal and Skin Diseases R01 AR073236 to JES, by the Faculty Seed
322 Grant from the Center for Engineering MechanoBiology (CEMB), an NSF Science and

323 Technology Center, under grant agreement CMMI: 15-48571. Any opinions, findings, and
324 conclusions or recommendations expressed in this material are those of the authors and do
325 not necessarily reflect the views of the National Science Foundation.

326

327 **Materials and Methods**

328 **Generation Fn1-fluorescent protein targeting constructs**

329 Sequences of monomeric (m) green fluorescent protein (GFP), mNeonGreen, mScarlet-I, and
330 tdTomato were obtained from FPbase (<https://www.fpbase.org>). The sequence encoding one
331 of the above fluorescent proteins (FPs) was knocked into the Fn1 locus following the last
332 coding exon of mouse Fn1, and separated from the last coding amino acid by a flexible,
333 proline-rich linker, PPPELLGGP (51). Targeting was achieved by CRISPR/Cas9 (52). The
334 sequence of the guide RNA was chosen and off-target sites were identified using GuideScan
335 and Off-Spotter software (53, 54). The guide RNA (gRNA) sequence 5'-AGC GGC ATG AAG
336 CAC TCA AT-3' targeting the last coding exon of *Fn1* was subcloned downstream the U6
337 promoter into the PX459 vector (Addgene, cat # 62988) encoding the Cas9-2A-Puromycin
338 cassette (52). The homology-directed repair (HDR) template was constructed using pBS-KS
339 vector (Sup. Fig. 1a). The sequence of the last coding exon of *Fn1* 5'-
340 AACGTAAATTGCCCCATTGAGTGCTTCATGCCGCTAGATGTGCAAGCTGACAGAGACGAT
341 TCTCGAGAG-3' was modified to 5'-
342 AACGTAAATTGCCCCATcGAaTGCTTCATGCCGCTAGATGTGCAAGCTGACAGAGACGATT
343 CTCGAGAG-3' in the HDR template by introducing silent mutations (underlined) to prevent
344 targeting of the template by the gRNA. Homology arm 1 contained 677 bp encoding exon #45,
345 intron, and a portion of the last exon (#46), of the transcript *ENSMUST00000055226.12*.
346 Homology arm 2 encoded 1739 bp immediately downstream of the *Fn1* termination codon and
347 included the unmodified 3'UTR of Fn1. Knockin Fn1^{mEGFP/+} mice were generated by

348 Biocytogen using the same HDR construct and a longer gRNA, 5'-TAG CGG CAT GAA GCA
349 CTC AAT GG-3',
350 targeting the same sequence in the last coding exon (differences between the two gRNAs are
351 underlined). Targeting was confirmed by sequencing and Southern Blotting
352 (Sub. Fig. 1b). 500 bp around each of the top ten predicted off-target sites were sequenced
353 and no mutations were found in the founder mice. Mice containing correctly-targeted *Fn1* locus
354 were used to establish living colonies of $Fn1^{mEGFP/mEGFP}$ animals. Mice were housed in an
355 AAALAC-approved barrier facility. All experimental procedures were approved by the
356 Institutional Animal Care and Use Committee of Rutgers University and conducted in
357 accordance with the Federal guidelines for the humane care of animals.

358

359 **Generation of Fn1-FP-expressing cell lines**

360 Mouse embryonic fibroblasts (MEFs) were isolated from embryonic day (E) 13.5 embryos
361 derived from the C57BL/6J strain (Jackson Labs, stock # 664) according to established
362 protocols (55) and cultured in high-glucose Dulbecco's Modified Eagle Medium (DMEM,
363 Corning, cat # 10-013-CV) supplemented with 10% v/v fetal bovine serum (Gemini
364 Biosciences, cat # 100-106), 1% v/v penicillin/streptomycin solution (GE Healthcare, cat
365 #SV30010), 1% v/v L-glutamine (Gibco, cat # 35050-061). We refer to this as complete
366 medium henceforth in the methods. CRISPR targeting was performed by transfecting the
367 PX459 plasmid encoding *Fn1* gRNA and the HDR template using lipofectamine 3000, as
368 described (52). For all other experiments, MEFs expressing *Fn1*-mEGFP proteins were
369 generated from E13.5 $Fn1^{mEGFP/+}$ embryos. Wild-type MEFs were isolated from the littermates
370 of $Fn1^{mEGFP/+}$ embryos.

371

372 **Analysis of Fn1 matrix assembly**

373 Matrix Assembly was performed according to the established protocols (22). MEFs were plated
374 in 6-well dishes (9 cm² growth area) at a density of 2×10^5 cells per well for 48 h, in complete
375 medium and incubated under sterile conditions at 37°C, 5% CO₂. Cells were washed twice
376 with ice cold PBS (supplemented with Mg²⁺ and Ca²⁺), scraped with a cell scraper and lysed
377 with either 500 µl RIPA lysis buffer pH 8.0 (50 mM Tris-Cl, 150 mM NaCl, 2 mM EDTA, 1% v/v
378 NP-40, 0.5% w/v sodium deoxycholate, 0.1% w/v SDS, 1X protease inhibitor cocktail (Cell
379 Signaling Technology, cat # 5871), or DOC lysis buffer, pH 8.8 (20 mM Tris-Cl, 2 mM EDTA,
380 2% w/v sodium deoxycholate, 1X protease inhibitor cocktail (Cell Signaling Technology, 5871)).
381 Extracts were carefully transferred to Eppendorf tubes containing 1 µl (250 units) Benzonase®
382 Nuclease (Sigma-Aldrich, E1014), mixed by inverting a few times and incubated at 37 °C for
383 15 mins. The samples were then centrifuged at 16,000 × g for 15 min at 4 °C. For cells lysed
384 with DOC lysis buffer, the supernatant containing DOC-soluble material was carefully
385 removed, and the pellet containing the DOC-insoluble material was resuspended in 100 µl
386 SDS solubilization buffer, pH8.8 (20 mM Tris-Cl, 2 mM EDTA, 1% w/v SDS, 1X protease
387 inhibitor cocktail (Cell Signaling Technology, 5871)). The DOC-insoluble pellet was thoroughly
388 dissolved by heating the sample to 95 °C and vortexing. All samples were aliquoted and stored
389 at -80 °C until further use. Prior to quantification of Fn1 in the samples, the total protein
390 concentration of the RIPA and DOC lysates was determined using the BCA protein assay
391 (Pierce™ BCA Protein Assay Kit, 23225). Fn1 and Fn1-FP fusion proteins were resolved using
392 66-440 kDa Wes separation module (ProteinSimple, SM-W007). Primary antibodies were used
393 at the following dilutions: anti-total Fn1 – 1:1000 (Abcam, ab199056), anti-GFP – 1:1000
394 (Roche, 11814460001), anti-mCherry – 1:1000 (Abcam, 167453). Primary antibodies were
395 detected using horseradish peroxidase-conjugated secondary antibodies (anti-Rabbit
396 Detection Module ProteinSimple, DM-001), and chemiluminescence was quantified using the

397 Compass for SW software (v3.1.8). Prior to running experimental samples, care was taken to
398 optimize the dilutions of lysates to be within the linear range of the detection.

399

400 **Chemicals and reagents**

401 Cells were grown in complete medium consisting of high-glucose Dulbecco's Modified Eagle
402 Medium (DMEM, Corning, cat # 10-013-CV) supplemented with 10% v/v fetal bovine serum
403 (Gemini Biosciences, cat # 100-106), 1% v/v penicillin/streptomycin solution (GE Healthcare,
404 cat #SV30010), 1% v/v L-glutamine (Gibco, cat # 35050-061). During live imaging cells were
405 incubated in FluoroBrite DMEM (Thermo Fisher Scientific, catalog # A1896701) supplemented
406 with 2% v/v fetal bovine serum (Gemini Biosciences 100-106), 1% v/v penicillin/streptomycin
407 solution (GE Healthcare, SV30010), 1% v/v L-glutamine (Gibco 35050-061). We refer to this as
408 imaging medium in the methods henceforth. The pH of the imaging medium was 8.14. FUD
409 and III-11C peptides were generated as described (31, 36) and stored in PBS at -80° C. 4%
410 DOC solution was prepared by dissolving 0.4 g deoxycholate salt (Sigma, catalog # D6750) in
411 10 ml of imaging medium; the solution was then vortexed and filter sterilized. The pH of the
412 final solution was 8.01. 16% paraformaldehyde (PFA) (Electron microscopy Sciences; catalog
413 # 50-980-487) was diluted in 1x PBS to prepare 4% PFA. The 4% PFA solution was aliquoted
414 into 1 ml microfuge tubes, stored at -80° C, and thawed at 37° C immediately before use.
415 Triton X-100 (100X stock, Sigma-Aldrich, catalog # T-8787) was used to prepare 1X PBST by
416 diluting in 10X PBS (VWR, catalog # 76180-740). Blocking buffer was prepared by adding 5%
417 Donkey serum (Sigma-Aldrich, catalog # D9663) to 1X PBST. 5 mg/ml stock of DAPI (Fisher
418 Scientific, cat #D3571) was prepared in water and used at 1:300 dilution. Stain Buffer (cat #
419 554656 BD Pharmingen) was used for antibody dilutions and washing of cells that were
420 stained without permeabilization. Hoechst 33342 Trihydrochloride, Thermo Fisher, catalog #
421 H1399, Stock- 10mg/ml, was used for labelling live MEFs at 1:300 dilution. In live MEFs, F-
422 actin was labelled using SiR actin (cat# CY-SC001 used at 1 μ M final concentration).

423 mCardinal-Lifeact-7 was a gift from Michael Davidson (Addgene plasmid # 54663 ;
424 <http://n2t.net/addgene:54663> ; RRID:Addgene_54663). Vectashield antifade mounting medium
425 (Vectorlabs, catalog # H-1000), was used for cover slipping. STORM buffer was prepared
426 using 50 mM Tris-HCl (fisher scientific, catalog # T-395-1), pH 8.0, 10 mM NaCl (Sigma-
427 Aldrich, catalog # S-7653), 10% glucose (Sigma- Aldrich, catalog # G8270), 0.5 mg/ml glucose
428 oxidase (Sigma- Aldrich, catalog # G2133), 40 μ g/ml catalase (Sigma- Aldrich, catalog # C40),
429 10 mM mercaptoethylamine (MEA, Sigma-Aldrich, catalog # 30070), according to (56).

430 **Cell plating and chambers**

431 All live imaging and STORM experiments were performed using Ibidi glass bottom 8-well
432 chambers (catalog # 80827) or MatTek round glass bottom dishes (catalog # P35G-1.5-14-C).
433 For imaging fixed cells, cells were plated on #1.5 round glass coverslips (Electron Microscopy
434 Sciences. Catalog # 72230-01). Coverslips were used either without coating or were coated
435 with the following ECM proteins: gelatin (Sigma Aldrich, catalog # G2500) (stock 0.1% in
436 distilled water), vitronectin (Sigma Aldrich, catalog # SRP3186; stock solution was prepared as
437 200 μ g/ml in 0.1% BSA and water) and laminin (R&D systems, catalog # 3400-010-02, stock 1
438 mg/ml was pipeted into 10ul aliquots and stored at -80°C). To coat with gelatin, glass surfaces
439 were incubated with the 0.1% gelatin solution for 5 min at room temperature (rt). To coat with
440 vitronectin or laminin, glass surfaces were incubated at 37° C for 1 hr in 20 μ g/ml of either
441 vitronectin or laminin, excess liquid was removed, cover slips were rinsed once with 1X PBS,
442 and blocked with 10 μ g/ml heat denatured BSA for 30 min before plating cells (14). Cells were
443 grown in complete medium. During live imaging cells were incubated in imaging medium.

444 **Antibodies**

445 All primary antibodies were checked for specificity on genetically-null tissues: Fn1-null tissue
446 sections obtained from Fn1-null embryos were used to assay the specificity of each of the anti-

447 Fn1 antibodies; Tissues isolated from GFP-null, Itga5-null, and mCherry-null embryos were
 448 used to check the specificity of anti-GFP, anti-Itga5, and anti-mCherry antibodies. For each of
 449 the antibodies, staining of control tissues resulted in no more fluorescent signal than the
 450 background fluorescence produced by the use of secondary antibodies only.

451

452 **Antibodies**

Primary Antibodies (Ab)	Source, catalog #, concentration	Dilution / ng used per staining
tFn monoclonal Ab	Abcam, cat # 199056, 0.429 mg/ml	1:300 for STORM, 429 ng
tFn polyclonal Ab, 297.1 serum	Richard Hynes lab	1:2000 for IF, 1:500 for STORM
Fn1 N-term, R184 serum	Jean Schwarzbauer's lab	1:2000 for IF, 1:25 for STORM
GFP	Aves lab, cat# GFP-1010, 30 µg/ml	1:300 for STORM / 30 ng
Itga5	BD biosciences, cat # 553319	1:100
mCherry	Abcam, cat # ab167453	1:100

453

Secondary Antibodies	Source, catalog #, concentration	Dilution/ µg of antibody in staining solution)
donkey anti-rabbit Alexa Fluor 647	Thermo Fisher Scientific, A-31573, 2 mg/ml	1:300 / 2 µg

donkey anti-mouse Alexa Fluor 555	Thermo Fisher Scientific, A-31570, 2 mg/ml	1:300 / 2 μ g
donkey anti-rat Alexa Fluor 555	Jackson Immunoresearch, 712-166-150, 1.5mg/ml	1:300 / 1.5 μ g
donkey anti-chicken Alexa Fluor 488	Jackson Immunoresearch, 703-546-155, 1.5mg/ml	1:300 / 1.5 μ g
donkey anti-chicken Alexa Fluor 647	Jackson Immunoresearch, 703-606-155, 1.5mg/ml	1:300 / 1.5 μ g

454

455 **Cell culture and treatments**

456 MEFs were maintained by plating on 25 cm² dishes (25 cm² growth area) in complete medium
457 and incubated under sterile conditions at 37°C, 5% CO₂. For FUD and III-11C treatment
458 Fn1^{mEGFP/+} MEFs were plated in 8-well glass Ibidi dishes (1 cm² growth area) without coating at
459 a density of 0.6x10⁴ cells/well in complete medium. After 5 hours, DMEM was removed and
460 cells were rinsed once with 1X PBS. Subsequently, the medium was changed to imaging
461 medium. For FUD experiments, imaging medium was supplemented either with 225 nM FUD
462 or 274 nM of control III-11C peptide. Untreated wells contained cells incubated with imaging
463 medium. Following the addition of the imaging medium (with or without the peptides), the
464 chamber was immediately set up for live imaging under in the humidified Tokai Hit stage-top
465 incubator at 37°C, 5% CO₂.

466

467 In order to enrich for non-fibrillar nanodomains, Fn1^{mEGFP/+} MEFs were plated in 8 well glass
468 Ibidi dishes (1 cm² growth area) without coating. Cell were plated at the density of 0.6x10⁴
469 cells/well in imaging medium with or without FUD (225 nM) or III-11C (274 nM), and incubated
470 in at 37°C, 5% CO₂ for 1 hr. Subsequently, MEFs were rinsed once in warm 1X PBS and fixed

471 using pre-warmed 4% PFA for 20 min. After fixation, wells were rinsed three times, 5 min each
472 with Stain Buffer (cat # 554656 BD Pharmingen), blocked for 30 min at room using 5% Donkey
473 serum prepared in Stain Buffer, and incubated with the monoclonal anti-Fn1 (Abcam, cat #
474 199056) overnight at 4° C. Cell were then rinsed with Stain Buffer three times, 10 min each,
475 and incubated with anti-rabbit antibodies conjugated with Alexa-647 for 1 hour at rt. Cell were
476 then rinsed again with Stain Buffer three times, 10 min each, and stored at 4° C in 1X PBS for
477 imaging later.

478

479 **Hydrogels**

480 **Methacrylated Alginate Synthesis:** Methacrylated alginate (MeAlg) was synthesized
481 according to a previously established protocol (57). In brief, alginic acid sodium salt from brown
482 algae (Sigma-Aldrich, USA) (3% w/v) was fully dissolved in Dulbecco's phosphate buffered
483 saline (dPBS, Sigma-Aldrich, USA). Then, methacrylic anhydride (Sigma-Aldrich, USA) (8% v/v)
484 was added drop-wise to the alginate solution and stirred for 12 h at 4°C, using 2M NaOH (Sigma-
485 Aldrich, USA) to ensure that the pH remained between 8 and 9 for the duration of the reaction.
486 The resulting solution was passed through filter paper (GE Whatman) and poured into
487 Spectra/Por dialysis membrane with a 6–8 kDa molecular weight cutoff (Fischer Scientific) and
488 kept in DIW under stirring for 7 days to eliminate the unreacted MA and salts. Dialyzed solution
489 was then freeze-dried for 4 days to obtain MeAlg foam.

490 **Fabrication of the Hydrogel Substrates:** MeAlg substrates were fabricated using a previously
491 established protocol (58). Briefly, petri dishes with glass bottoms were treated with UV/ozone
492 (UVO) for 30 minutes, immediately followed by a coating of 3-(trimethoxysilyl)propyl
493 methacrylate (TMS) (Sigma-Aldrich, USA) to methacrylate the glass surfaces (59). The dishes
494 were left in a desiccator overnight. The hydrogels were fabricated using Michael-type addition
495 polymerization. First, 2-hydroxy-4'-(2-hydroxyethoxy)-2-methylpropiophenone (I2959) (Sigma-

496 Aldrich, USA), a photoinitiator (0.5% w/v) was completely dissolved in Dulbecco's PBS (dPBS),
497 followed by the lyophilized MeAlg (3% w/v) synthesized previously. This was kept at room
498 temperature until a clear solution was achieved. Crosslinking occurs with the introduction of DL-
499 Dithiothreitol (DTT) (Sigma-Aldrich, USA) to the solution, along with 0.2M triethanolamine
500 (Sigma-Aldrich, USA) at pH 10. To form 3kPa and 12 kPa gels, 20% and 30% (w/v) DTT are
501 used, respectively. To promote cell adhesion, GRGDSPC peptide (1% w/v) (Genscript) was
502 added to the solution. After all contents were thoroughly mixed, 5 μ L of MeAlg solution was
503 pipetted onto the surface of the dish before being covered with a glass coverslip in order to
504 create gels less than 30 μ m thick. These were left at room temperature for an hour to crosslink
505 before being submerged in dPBS to remove the coverslip.

506 **Atomic Force Microscopy:** For stiffness measurements, hydrogel samples were submerged in
507 dPBS and placed in a Dimension Icon AFM with ScanAsyst (Bruker). Using the PeakForce-
508 QNM mode, hydrogel samples were indented using an MLCT-Bio probe tip with pyramidal
509 geometry (Bruker, CA) and a nominal spring constant of 0.03 N/m, checked by thermal
510 calibration.

511

512 **Treatment of cells with Deoxycholate (DOC)**

513 10^4 Fn1^{mEGFP/+} MEFs were plated for 48 hrs in 8-well glass bottom Ibidi dishes in complete
514 medium and incubated at 37°C and 5% CO₂. Two hours before imaging SiR-actin was added
515 at 1 μ M final concentration. SiR-actin contains a far-red dye, silicon rhodamine, conjugated to
516 jasplakinolide that labels F-actin in live and fixed cells (60). Just before imaging, complete
517 medium was replaced by 150 μ l imaging medium containing 33 μ g/ml of Hoechst 33342.
518 Positions were marked in each well and live imaging was initiated at 37°C and 5 % CO₂
519 humidified chamber. After 15 min, 150 μ l 4% DOC solution prepared in imaging medium
520 containing 33 μ g/ml Hoechst was added to the experimental well (final pH 8.01) and 150 μ l

521 imaging medium containing 33 $\mu\text{g/ml}$ Hoechst but without DOC was added to the control well.
522 Cells were imaged at 50 sec intervals until F-actin and DNA disappeared (see Movie 4). The
523 medium was then removed, cells were rinsed for 1 min with 1X PBS pre-warmed to 37°C, fixed
524 with 4% PFA pre-warmed to 37°C, and stained to detect Fn1, as described below.

525

526 **Immunofluorescence staining of permeabilized cells**

527 MEFs were grown either on #1.5 round glass coverslips in 24-well dishes or in 8-well glass
528 Ibidi dishes depending on the experiment for the times indicated in figure legends. MEFs were
529 then rinsed with 1X PBS (warmed to 37⁰ C) for 5 min, fixed with freshly thawed 4% PFA pre-
530 warmed to 37⁰ C for 20 min, and washed three times with 1X PBS (warmed to 37⁰ C) with mild
531 shaking. All subsequent washing steps were done with shaking. For permeabilization, cells
532 were washed once in 1X PBS containing 0.1% Triton- X 100 (PBST). Blocking was done for 30
533 min in 5% Donkey serum prepared in PBST (blocking solution). After blocking, cells were
534 incubated in primary antibodies were diluted in blocking solution overnight at 4⁰ C, as specified
535 in the table above. This was followed by 3 washes in PBST for 10 min each. Cells were then
536 incubated with secondary antibodies diluted in PBST for 60 min at rt. Finally, cells were
537 washed three times with PBST for 10 min each. DAPI (1:300) was added to the second wash.
538 Cells were mounted using Vectashield.

539

540 **Imaging**

541 Fixed samples on coverslips and 8-well Ibidi dishes were imaged using Nikon A1-HD25
542 inverted confocal microscope with the DUG 4-Channel Detector and 2 GaAsP, 2 high-
543 sensitivity PMTs, and a motorized XYZ stage with Nikon's Perfect Focus 4 system. Plan Fluor
544 40x Oil (numerical aperture 1.3, cat # MRH01401) was used for live imaging, and CFI

545 Apochromat TIRF 100xC Oil objective with numerical aperture 1.49 (cat # MRD01905) was
546 used with the enhanced resolution protocol, TIRF, and STORM.

547

548 **Confocal Settings**

549 Confocal images of fixed samples were recorded using Nikon A1-HD25 inverted confocal
550 microscope equipped with CFI Apochromat TIRF 100xC Oil objective with the pinhole set to
551 0.8 Airy units, and imaged through 2 – 4 microns with step size of 0.125 μm - 0.15 μm at a
552 sampling of 40 nm per pixel. Crop function was used to reduce imaging time and sample
553 bleaching. Deconvolution was done using Nikon 3D deconvolution software (v5.11.01).

554 Airyscan imaging was performed using Zeiss LSM 880 fitted with a 32 array AiryScan GaAsP-
555 PMT detector and the Plan Apochromat 63X Oil (NA 1.4) objective. Deconvolution and pixel
556 reassignment were done using Zeiss LSM software.

557

558 **Live imaging**

559 Ibidi 8-well glass-bottom slides or MatTek glass bottom dishes were placed into humidified
560 Tokai Hit stage-top incubator maintained at 37° C and a 5% CO₂ atmosphere. mEGFP was
561 excited using 488 nm laser at 1% power and pinhole set to 1 Airy unit. An optical zoom of 2
562 and Z step size of 0.5 μm were used, and stack size was set to 10-15 microns allowing to
563 image the entire cell. For overnight movies, each position was filmed every 1.5 min – 4 min, as
564 noted in Movie legends, for the DOC assay, imaging was performed at 54 sec intervals.

565

566 **Movies**

567 Movies in the mp4 format were generated using Imaris 9.5.1 (Bitplane), titles and arrows were
568 added using Adobe Premiere Elements Editor 2020.

569

570 **TIRF imaging**

571 TIRF microscopy was performed using Nikon A1-HD25 inverted confocal microscope equipped
572 with 4 laser lines of 100mW per line at 405, 488, and 561nm and 125mW at 640nm, and
573 motorized TIRF illumination. CFI Apochromat TIRF 100xC Oil objective and EMCCD camera
574 were used. Before imaging lasers were aligned and the critical angle of incidence for imaging
575 was determined by the software. The exposure time was 20 ms and readout speed was set at
576 10 MHz.

577

578 **STORM imaging**

579 Following IF staining, primary antibodies were detected using secondary antibodies coupled
580 with Alexa-647 fluorescent dye. Samples were washed and stored in PBS at 4°C. Prior to
581 imaging, freshly prepared STORM buffer was added and the chamber was immediately sealed
582 using parafilm. STORM was performed using Nikon A1-HD25 Ti2E microscope equipped with
583 motorized TIRF illumination, 125mW 640 nm solid-state laser, Perfect Focus, and a
584 100x/1.49NA objective. Images were acquired at the critical angle of incidence and recorded
585 using a 512 x 512 EMCCD camera (Princeton Instruments). Calibration, drift correction, and z-
586 rejection were based on the calibration file obtained by imaging of 100 nm Tetraspeck beads
587 (Life technologies, catalog # T-7279) using the same glass surface and buffer conditions. To
588 drive Alexa-647 into the dark state, samples were pre-bleached by the illumination at 640 nm
589 for 10 seconds at 100 % laser power. Images were acquired for 40,000 frames at 8.4 ms
590 exposure. Blinking events were fitted using the Nikon N-STORM localization software. Images
591 in which the Gaussian distribution of spot sizes was centered at 2 – 5 nm were used for further
592 analyses. Localization events with fewer than 800 or more than 50000 photons were filtered
593 out to remove blinking events that were either too faint or too bright. In addition, blinking events
594 were filtered out if they occurred in more than 3 consecutive periods or where outside the z-

595 range determined by the calibration using 100 nm Tetraspeck beads. Images in which z-
596 rejection was below 50% were used for the analyses.

597

598 **Analysis of the number of molecules within non-fibrillar and fibrillar Fn1 nanodomains**

599 The free-hand ROI tool in the STORM window (Nikon Elements AR Software v5.11.01) was
600 used to draw ROI around nanodomains in fibrils or non-fibrillar nanodomains in a fibril to get a
601 count of molecule numbers. Fn1 nanodomains were analyzed in 5 random regions from 3
602 independently acquired images (a total of 15 fields) for each sample/antibody type. To
603 determine the molecule number in Fn1 nanodomains within fibrils, we analyzed more than 20
604 fibrils per antibody, from 3 or more independently acquired images. All the counts were plotted
605 in Prism 8.2.1 (GraphPad Software, USA), and compared using either one-way ANOVA test
606 with Tukey's correction or Kruskal-Wallis test with Dunn's correction for multiple testing.

607

608 **Analysis of distance between fluorescence Fn1 nanodomains in fibrils** Distances

609 between nanodomains were quantified by measuring the distance between the centers of
610 nanodomain within fibrils using Nikon image analysis software and by Fiji peak analysis plugin,
611 which was done in the following manner: In order to quantify distance between nanodomains in
612 a fibril, a snapshot of the STORM window was generated. Rectangular ROI box was drawn
613 around a fibril and plot profiles were generated. We analyzed more than 20 thin fibrils from 3 or
614 more independently acquired images for each antibody type. Plot profiles were analyzed using
615 Find Peak function in the BAR module of Fiji (Tiago Ferreira et al., (2016)
616 10.5281/zenodo.28838). Default settings were used to generate lists of maxima and minima
617 for each plot. Lists were extracted to Microsoft Excel and distances between peak maxima
618 were computed. Distances measured manually and automatically were comparable and all
619 were plotted using Prism 8.2.1. See **Supplemental Figure 5a** for the automatic peak finding
620 workflow.

621

622 **Analysis of distance between non-fibrillar nanodomains** In order to quantify distance
623 between non-fibrillar nanodomains in an image, a snapshot of the STORM window was
624 generated. Rectangular ROI box used for analysis of distance between density peaks in a fibril
625 was reloaded and positioned to capture as many non-fibrillar nanodomains as possible in a
626 rectangle. More than 5 regions from 3 or more independently acquired images were analyzed
627 for Fn1^{mEGFP/+} MEFs immunostained with a cocktail of four antibodies, anti-N-terminal Fn1
628 antibody, monoclonal anti-tFn1, polyclonal anti-tFn1, and anti-GFP antibodies. Plot profiles
629 were analyzed using Find Peak function in the BAR module of Fiji ((Tiago Ferreira et al.,
630 (2016) 10.5281/zenodo.28838). Default settings were used to generate lists of maxima and
631 minima for each plot. Lists were extracted to Microsoft Excel and distances between peak
632 maxima were computed. Distances were plotted using Prism 8.2.1. See **Supplemental Figure**
633 **5B** for the workflow.

634

635 **Analysis of area and diameter of non-fibrillar and fibrillar nanodomains** Snapshots of 5
636 regions were generated from 3 independently acquired images and saved as .png files with
637 scale bars. Images were converted to 8-bit files and thresholded in Fiji. “Analyze particle”
638 function was used to extract the area for all nanodomains in the image. These values were
639 copied into an excel file where they were sorted from largest to smallest. Areas smaller than
640 $10^{-4} \mu\text{m}^2$ (~11.9 nm in diameter) were excluded from the analyses (see **Supplemental Figure**
641 **6A-C**). There were no statistical differences between non-fibrillar nanodomain areas of
642 untreated, FUD- or 11-IIC treated cells without filtering (**Supplemental Figure 6D-E**). The
643 values for nanodomain diameters were extracted from the area measurements and confirmed
644 manually for a smaller sample, by measuring nanodomain diameters using the Nikon software.

645

646

647 **Figure Legends**

648 **Figure 1. Beaded architecture of Fn1 fibrils in embryonic ECM.** Wild-type E9.5 mouse
649 embryos were fixed and stained with the monoclonal antibody to Fn1 (white) and DAPI, and
650 imaged using 100x oil objective, N.A. 1.49, pinhole 0.8, and sampling rate of 40 nm/pixel. **A –**
651 **A1.** Sagittal optical section through the first pharyngeal arch and **b.** the cardiac jelly, an ECM-
652 rich region between the myocardial and endocardial layers of the outflow tract of the heart.
653 Large arrowheads in **A – A1** point to the ECM at the ectoderm-mesenchyme boundary of the
654 1st pharyngeal arch. The box in **(A)** is expanded in **A1** to show the beaded Fn1
655 microarchitecture. Arrow in **A1** points to Fn1 fibril within the arch mesenchyme; **B.** Beaded
656 architecture of Fn1 fibrils in cardiac jelly, e.g., arrow. **C.** Intensity profile plot of a Fn1 fibril
657 shows a regularly-undulating profile, with peaks corresponding with Fn1 “beads”; a.u. arbitrary
658 units.

659

660 **Figure 2. Integrin $\alpha 5\beta 1$ and Fn1 co-localize in beaded adhesions.** Wild-type MEFs were
661 plated for 16 hours on glass coverslips, then fixed, stained with antibodies to Fn1 and integrin
662 $\alpha 5$ (Itga5), and imaged at the critical angle of incidence using 100x oil objective, NA 1.49. **A –**
663 **A2** cell periphery. Arrows in **A – A2** point to examples of non-fibrillar Fn1 adhesions (“beads”)
664 at cell periphery. **B - B2** medial portion of a cell containing beaded fibrillar adhesions (arrows).
665 Note that both Itga5 and Fn1 stainings are beaded. Magnifications in all panels are the same.

666

667 **Figure 3. Beaded architecture of Fn1 fibrils is present in fibrils between cells and is**
668 **retained in the absence of cell contact.** **A – B.** Fn1 secreted by wild-type MEFs and
669 deposited **A)** on glass or **B)** between cells. **C.** Fn1 fibrils between endothelial cells. Boxes in
670 **A– C** are magnified in **A1-C1**. Arrows point to fibrils left behind on substrata (**A1**) or between
671 cells (**B1-C1**). **d.** Fn1^{Neon Green} MEFs were treated with 2% DOC pH 8 until cells were dissolved

672 (see Movie 3). Following DOC treatment, Fn1 was imaged using 100x oil objective, NA 1.49,
673 pinhole size 0.8 Airy units, and sampling resolution of 40 nm/pixel in x,y. Note beaded
674 architecture (arrows).

675

676 **Figure 4. Fn1 fibrils are composed linear arrays of Fn1 nanodomains.** Fn1^{mEGFP/+} MEFs
677 were plated on glass for 16 hrs, then fixed and stained with antibodies to GFP followed by
678 secondary antibodies conjugated to Alexa-647. **A.** Native GFP fluorescence imaged by TIRF
679 using 100x objective NA 1.49. Arrow in **A** points to a thin, beaded Fn1 fibril resolved by
680 STORM in **B1**, **B1'** and **B2**. **B.** The entire field of view in **A** is imaged by STORM detecting
681 Alexa-Fluor 647-conjugated antibody (see Methods). The box in **B** is expanded in **B1**. The box
682 in **B1** is expanded in **B2**. The arrow in **B1** points to the same region as the arrow in **A**. Arrows
683 in **B2** point to Fn1 nanodomains; arrowheads point to Fn1 localizations between the
684 nanodomains, notched arrowheads point to Fn1 nanodomains that are not in fibrils and wide
685 arrows point to Fn1-free areas between the nanodomains in the fibril marked by the arrow in **A**.

686

687 **A, B, B1, B1'** and **B2** are in x-y planes; **B2'** shows the nanodomains in **B2** in the x-z plane.

688 Images in **B1'** and **B2'** are depth-coded according to the scale in **B1'**. See Movie 4 for 3D
689 rotation of the fibril underlined in **B1'** around the x-axis.

690 **Figure 5. Fn1 fibrils are composed of nanodomains containing multiple Fn1 dimers.**

691 Wild-type or Fn1^{mEGFP/+} MEFs were plated on glass for 16 hrs, fixed and stained with different
692 antibodies to Fn1 followed by Alexa 647-conjugated secondary antibodies. Columns showing
693 cells treated with DOC prior to fixation are marked. Cells were imaged using STORM. **A.**
694 zoom-out views to show the overall appearance of Fn1 fibrils. **B-E.** Successive magnifications
695 of fibrils shown in **(A)**. Arrows in **D** point to nanodomains magnified in **E**; arrowheads in **D-E**
696 point to Fn1 molecules between nanodomains, wide open arrows point to Fn1-free zones
697 between nanodomains in a fibril. **F.** distances between nanodomains within fibrils or non-

698 fibrillar (NF) nanodomains, **** $p < 10^{-4}$, Kruskal-Wallis test, with Dunn's correction for multiple
699 testing. Inset in **F** is a plot profile of the fibril marked by the box in the column **6D** showing
700 regularly-spaced peaks of intensity. DOC-treated samples are marked. 4-antibody cocktail
701 contains four antibodies as in **Model 1**. **G**. Diameter of nanodomains in fibrils. **H**. number of
702 Fn1 localizations per nanodomain in fibrils. **Model 1**. Two Fn1 dimers in a fibril. Depiction of
703 antibody coverage of Fn1 fibrils if dimers were oriented in end-to-end fashion with alternating
704 N- and C-termini. **Model 2**. Our data show that Fn1 fibrils consist of a linear array of
705 nanodomains (black arrows) containing multiple Fn1 dimers (Fn1 dimers are depicted as balls
706 and color-coded according to the antibody scheme in **Model 1**. Arrowheads point to Fn1 and
707 open arrows point to Fn1-free areas between nanodomains.

708

709 **Figure 6. The N-terminal Fn1 assembly domain regulates the organization of Fn1**
710 **nanodomains into linear fibrillar arrays.** Fn1^{mEGFP/+} MEFs were plated on glass and were
711 either left untreated, or were incubated with the control 11-IIIC peptide, or the FUD peptide for
712 16 hrs. Cells were then fixed and stained with the monoclonal antibody to Fn1 followed by Alexa
713 647-conjugated secondary antibodies. Cells were imaged at the critical angle of incidence by
714 STORM. **A – A2**. Untreated, unpermeabilized cells. **B – B2**. Cells incubated with controls 11-
715 IIIC peptide. **C – C1, C1-1** FUD-treated, unpermeabilized cells. Boxes marked 1 in **A-B** were
716 expanded in **A1-B1**. Boxes marked 2 in **A-B**, were expanded in **A2 – B2**. The box in **C** is
717 expanded in **C1** and **C1-1**. Arrows in **A1-B1** point to Fn1 nanodomains (NDs) in fibrils. Arrows
718 in **C1** points to non-fibrillar nanodomains expanded in **C1-1**; **D**. Quantification of the number of
719 Fn1 localizations in NDs in fibrils and in non-fibrillar NDs after various conditions. Red lines
720 mark medians. Differences are not statistically significant, Kruskal-Wallis test with Dunn's
721 correction for multiple testing. **E**. Model of fibril formation: Fn1 dimers assemble into small
722 nanodomains containing integrin $\alpha 5\beta 1$ at cell periphery, move rearward with actin flow, and

723 become organized into linear arrays of nanodomains. Joining of the additional Fn1
724 nanodomains to these arrays leads to the generation of longer fibrils as the assembly moves
725 toward the cell center. FUD does not interfere with the formation of Fn1 nanodomains. But
726 instead, it blocks the organization of Fn1 nanodomains into linear arrays.

727

728 **Legends for Movies**

729 **Movie 1. Rotational views through the Fn1+ ECM in the cardiac jelly.** Whole E9.5 embryo
730 was stained using rabbit monoclonal anti-Fn1 antibody and imaged using 100x objective, N.A.
731 1.49, with the pinhole set at 0.8 Airy units, and sampling of 40 nm per pixel in x, y. The movie
732 shows 3D reconstruction through 3.4 μm of tissue sampled every 0.121 μm in z. Fn1 is in
733 white, DAPI is in blue. Arrows point to examples of beaded Fn1 fibrils.

734

735 **Movie 2. Fn1 fibrillogenesis imaged by TIRF microscopy.** Fn1^{mEGFP} MEFs were transiently
736 transfected with mCardinal-lifeact, plated on gelatin-coated glass cover slips, and imaged 48
737 hours later. Filming was done every 2 min for 30 min using TIRF and 100x objective, N.A.
738 1.49. The first set shows Fn1-mEGFP channel. Yellow arrows point to centripetally-moving
739 Fn1 nanodomains that appear to be organizing into an elongating linear fibril. The second set
740 is an overlay between Fn1-mEGFP and mCardinal-lifeact.

741

742 **Movie 3. 2% DOC dissolved cytoplasm and nucleus in under 13 min leaving Fn1 fibrils.**
743 MEFs expressing Fn1-mEGFP were plated on glass-bottom slides and labeled with SiRActin
744 (magenta) to visualize F-actin and Hoechst (blue) to visualize DNA. Time lapse was recorded
745 every 54 sec immediately following the addition of DOC solution, pH 8.01, to live cells. The
746 addition of 2% DOC dissolves actin cytoskeleton and nuclei, and leaves Fn1 ECM fibrils

747 (green). Fn1 fibrils collapse following the dissolution of the actin cytoskeleton due to the loss of
748 tension.

749

750 **Movie 4. 3D-rendering of STORM data.** Fn1 fibril underlined in Fig. 4b1 is rotated around the
751 x-axis to show the arrangement of Fn1 localizations in 3D. The movie starts in x-y plane.

752 Yellow arrows point at Fn1 nanodomains in the fibrils. Red arrows point to the space between
753 the nanodomains.

754

755 **Movie 5. Cells incubated with 11-IIIC, show robust fibrillogenesis.** Fn1^{mEGFP} MEFs were
756 plated on glass in 8-well Ibidi chambers for 4 hours, Medium containing 11-IIIC control peptide
757 was then added and cells were filmed every 90 sec for about 15 hours, as described in
758 Methods. The movie begins approximately 30 min after the 11-IIIC-containing medium was
759 added, the time it takes to set up time-laps recording. Arrows point to cell periphery and
760 examples of centripetally moving Fn1 fibrils.

761

762 **Movie 6. FUD interferes with linking centripetally moving Fn1+ nanodomains into fibrils.**

763 Fn1^{mEGFP} MEFs were plated on glass in 8-well Ibidi chambers for 4 hours. Medium containing
764 FUD peptide was then added and cells were filmed every 3 min for about 15 hours, as
765 described in Methods. The movie begins approximately 30 min after the FUD-containing
766 medium was added, the time it takes to set up time-laps recording. Note the dismantling of pre-
767 existing fibrils at the beginning of the movie. Yellow and red arrows point to cell periphery.
768 Note the presence of centripetally moving Fn1-mEGFP “beads” and the scarcity of Fn1 fibrils
769 for the majority of the duration of the movie.

770

771 References

- 772 1. J. E. Schwarzbauer, D. W. DeSimone, Fibronectins, their fibrillogenesis, and in vivo
773 functions. *Cold Spring Harbor perspectives in biology* **3** (2011).
- 774 2. T. Rozario, B. Dzamba, G. F. Weber, L. A. Davidson, D. W. DeSimone, The physical
775 state of fibronectin matrix differentially regulates morphogenetic movements in vivo. *Dev Biol*
776 **327**, 386-398 (2009).
- 777 3. P. Singh, J. E. Schwarzbauer, Fibronectin matrix assembly is essential for cell
778 condensation during chondrogenesis. *J Cell Sci* **127**, 4420-4428 (2014).
- 779 4. H. Y. Chiang, V. A. Korshunov, A. Serour, F. Shi, J. Sottile, Fibronectin is an important
780 regulator of flow-induced vascular remodeling. *Arterioscler Thromb Vasc Biol* **29**, 1074-1079
781 (2009).
- 782 5. X. Zhou *et al.*, Fibronectin fibrillogenesis regulates three-dimensional neovessel
783 formation. *Genes Dev* **22**, 1231-1243 (2008).
- 784 6. M. L. Smith *et al.*, Force-induced unfolding of fibronectin in the extracellular matrix of
785 living cells. *PLoS Biol* **5**, e268 (2007).
- 786 7. Q. Zhang, W. J. Checovich, D. M. Peters, R. M. Albrecht, D. F. Mosher, Modulation of
787 cell surface fibronectin assembly sites by lysophosphatidic acid. *J Cell Biol* **127**, 1447-1459
788 (1994).
- 789 8. Q. Zhang, M. K. Magnusson, D. F. Mosher, Lysophosphatidic acid and microtubule-
790 destabilizing agents stimulate fibronectin matrix assembly through Rho-dependent actin stress
791 fiber formation and cell contraction. *Mol Biol Cell* **8**, 1415-1425 (1997).
- 792 9. C. Zhong *et al.*, Rho-mediated contractility exposes a cryptic site in fibronectin and
793 induces fibronectin matrix assembly. *J Cell Biol* **141**, 539-551 (1998).
- 794 10. M. A. Chernousov, A. I. Faerman, M. G. Frid, O. Printseva, V. E. Kotliansky,
795 Monoclonal antibody to fibronectin which inhibits extracellular matrix assembly. *FEBS Lett* **217**,
796 124-128 (1987).
- 797 11. B. Geiger, A. Bershadsky, R. Pankov, K. M. Yamada, Transmembrane crosstalk
798 between the extracellular matrix--cytoskeleton crosstalk. *Nature reviews. Molecular cell biology*
799 **2**, 793-805 (2001).
- 800 12. B. Geiger, K. M. Yamada, Molecular architecture and function of matrix adhesions. *Cold*
801 *Spring Harb Perspect Biol* **3** (2011).
- 802 13. E. Zamir *et al.*, Dynamics and segregation of cell-matrix adhesions in cultured
803 fibroblasts. *Nat Cell Biol* **2**, 191-196 (2000).
- 804 14. J. Lu *et al.*, Basement Membrane Regulates Fibronectin Organization Using Sliding
805 Focal Adhesions Driven by a Contractile Winch. *Dev Cell* **52**, 631-646 e634 (2020).

- 806 15. R. Pankov *et al.*, Integrin dynamics and matrix assembly: tensin-dependent
807 translocation of alpha(5)beta(1) integrins promotes early fibronectin fibrillogenesis. *J Cell Biol*
808 **148**, 1075-1090 (2000).
- 809 16. E. Zamir *et al.*, Molecular diversity of cell-matrix adhesions. *J Cell Sci* **112 (Pt 11)**,
810 1655-1669 (1999).
- 811 17. S. M. Fruh, I. Schoen, J. Ries, V. Vogel, Molecular architecture of native fibronectin
812 fibrils. *Nat Commun* **6**, 7275 (2015).
- 813 18. B. J. Dzamba, D. M. Peters, Arrangement of cellular fibronectin in noncollagenous fibrils
814 in human fibroblast cultures. *J Cell Sci* **100 (Pt 3)**, 605-612 (1991).
- 815 19. Y. Chen, L. Zardi, D. M. Peters, High-resolution cryo-scanning electron microscopy
816 study of the macromolecular structure of fibronectin fibrils. *Scanning* **19**, 349-355 (1997).
- 817 20. M. G. Choi, R. O. Hynes, Biosynthesis and processing of fibronectin in NIL.8 hamster
818 cells. *J Biol Chem* **254**, 12050-12055 (1979).
- 819 21. P. Singh, C. Carraher, J. E. Schwarzbauer, Assembly of fibronectin extracellular matrix.
820 *Annu Rev Cell Dev Biol* **26**, 397-419 (2010).
- 821 22. I. Wierzbicka-Patynowski, Y. Mao, J. E. Schwarzbauer, Analysis of fibronectin matrix
822 assembly. *Current protocols in cell biology / editorial board, Juan S. Bonifacino ... [et al.]*
823 **Chapter 10**, Unit 10 12 (2004).
- 824 23. P. J. McKeown-Longo, D. F. Mosher, Binding of plasma fibronectin to cell layers of
825 human skin fibroblasts. *J Cell Biol* **97**, 466-472 (1983).
- 826 24. J. H. Peters, R. O. Hynes, Fibronectin isoform distribution in the mouse. I. The
827 alternatively spliced EIIIB, EIIIA, and V segments show widespread codistribution in the
828 developing mouse embryo. *Cell Adhes Commun* **4**, 103-125 (1996).
- 829 25. A. Jimenez, K. Friedl, C. Leterrier, About samples, giving examples: Optimized Single
830 Molecule Localization Microscopy. *Methods* **174**, 100-114 (2020).
- 831 26. K. Skorstengaard, M. S. Jensen, P. Sahl, T. E. Petersen, S. Magnusson, Complete
832 primary structure of bovine plasma fibronectin. *Eur J Biochem* **161**, 441-453 (1986).
- 833 27. M. E. Vega, B. Kastberger, B. Wehrle-Haller, J. E. Schwarzbauer, Stimulation of
834 Fibronectin Matrix Assembly by Lysine Acetylation. *Cells* **9** (2020).
- 835 28. S. Rickelt, R. O. Hynes, Antibodies and methods for immunohistochemistry of
836 extracellular matrix proteins. *Matrix Biol* **71-72**, 10-27 (2018).
- 837 29. J. E. Schwarzbauer, Identification of the fibronectin sequences required for assembly of
838 a fibrillar matrix. *J Cell Biol* **113**, 1463-1473 (1991).
- 839 30. J. L. Sechler *et al.*, A novel fibronectin binding site required for fibronectin fibril growth
840 during matrix assembly. *J Cell Biol* **154**, 1081-1088 (2001).

- 841 31. B. R. Tomasini-Johansson *et al.*, A 49-residue peptide from adhesin F1 of
842 *Streptococcus pyogenes* inhibits fibronectin matrix assembly. *J Biol Chem* **276**, 23430-23439
843 (2001).
- 844 32. A. Morla, Z. Zhang, E. Ruoslahti, Superfibronectin is a functionally distinct form of
845 fibronectin. *Nature* **367**, 193-196 (1994).
- 846 33. J. L. Sechler, Y. Takada, J. E. Schwarzbauer, Altered rate of fibronectin matrix
847 assembly by deletion of the first type III repeats. *J Cell Biol* **134**, 573-583 (1996).
- 848 34. M. S. Filla, K. D. Dimeo, T. Tong, D. M. Peters, Disruption of fibronectin matrix affects
849 type IV collagen, fibrillin and laminin deposition into extracellular matrix of human trabecular
850 meshwork (HTM) cells. *Exp Eye Res* **165**, 7-19 (2017).
- 851 35. L. M. Maurer *et al.*, Extended binding site on fibronectin for the functional upstream
852 domain of protein F1 of *Streptococcus pyogenes*. *J Biol Chem* **285**, 41087-41099 (2010).
- 853 36. J. Sottile, J. Chandler, Fibronectin matrix turnover occurs through a caveolin-1-
854 dependent process. *Mol Biol Cell* **16**, 757-768 (2005).
- 855 37. R. Y. Tsien, The green fluorescent protein. *Annual review of biochemistry* **67**, 509-544
856 (1998).
- 857 38. C. K. Choi *et al.*, Actin and alpha-actinin orchestrate the assembly and maturation of
858 nascent adhesions in a myosin II motor-independent manner. *Nat Cell Biol* **10**, 1039-1050
859 (2008).
- 860 39. C. H. Damsky, K. A. Knudsen, D. Bradley, C. A. Buck, A. F. Horwitz, Distribution of the
861 cell substratum attachment (CSAT) antigen on myogenic and fibroblastic cells in culture. *J Cell*
862 *Biol* **100**, 1528-1539 (1985).
- 863 40. F. Zhang, S. Saha, A. Kashina, Arginylation-dependent regulation of a proteolytic
864 product of talin is essential for cell-cell adhesion. *J Cell Biol* **197**, 819-836 (2012).
- 865 41. D. M. Peters, L. M. Portz, J. Fullenwider, D. F. Mosher, Co-assembly of plasma and
866 cellular fibronectins into fibrils in human fibroblast cultures. *J Cell Biol* **111**, 249-256 (1990).
- 867 42. L. M. Maurer, W. Ma, D. F. Mosher, Dynamic structure of plasma fibronectin. *Crit Rev*
868 *Biochem Mol Biol* **51**, 213-227 (2015).
- 869 43. W. Ma, H. Ma, D. F. Mosher, On-Off Kinetics of Engagement of FNI Modules of Soluble
870 Fibronectin by beta-Strand Addition. *PLoS One* **10**, e0124941 (2015).
- 871 44. Y. Arai *et al.*, Tying a molecular knot with optical tweezers. *Nature* **399**, 446-448 (1999).
- 872 45. A. M. Saitta, P. D. Soper, E. Wasserman, M. L. Klein, Influence of a knot on the strength
873 of a polymer strand. *Nature* **399**, 46-48 (1999).
- 874 46. T. Ohashi, D. P. Kiehart, H. P. Erickson, Dynamics and elasticity of the fibronectin
875 matrix in living cell culture visualized by fibronectin-green fluorescent protein. *Proc Natl Acad*
876 *Sci U S A* **96**, 2153-2158 (1999).

- 877 47. E. S. Wijelath *et al.*, Novel Vascular Endothelial Growth Factor Binding Domains of
878 Fibronectin Enhance Vascular Endothelial Growth Factor Biological Activity. *Circulation*
879 *research* **91**, 25-31 (2002).
- 880 48. M. M. Martino, J. A. Hubbell, The 12th-14th type III repeats of fibronectin function as a
881 highly promiscuous growth factor-binding domain. *FASEB J* **24**, 4711-4721 (2010).
- 882 49. J. T. Saunders, J. E. Schwarzbauer, Fibronectin matrix as a scaffold for procollagen
883 proteinase binding and collagen processing. *Mol Biol Cell* **30**, 2218-2226 (2019).
- 884 50. R. O. Hynes, The extracellular matrix: not just pretty fibrils. *Science* **326**, 1216-1219
885 (2009).
- 886 51. S. Snitkovsky, J. A. Young, Cell-specific viral targeting mediated by a soluble retroviral
887 receptor-ligand fusion protein. *Proc Natl Acad Sci U S A* **95**, 7063-7068 (1998).
- 888 52. F. A. Ran *et al.*, Genome engineering using the CRISPR-Cas9 system. *Nat Protoc* **8**,
889 2281-2308 (2013).
- 890 53. V. Pliatsika, I. Rigoutsos, "Off-Spotter": very fast and exhaustive enumeration of
891 genomic lookalikes for designing CRISPR/Cas guide RNAs. *Biol Direct* **10**, 4 (2015).
- 892 54. A. R. Perez *et al.*, GuideScan software for improved single and paired CRISPR guide
893 RNA design. *Nat Biotechnol* **35**, 347-349 (2017).
- 894 55. R. Behringer, M. Gertsenstein, K. Vintersten, A. Nagy, *Manipulating the Mouse Embryo:*
895 *A Laboratory Manual* (Cold Spring Harbor Laboratory Press, New York, ed. 4th, 2014), pp.
896 814.
- 897 56. G. T. Dempsey, J. C. Vaughan, K. H. Chen, M. Bates, X. Zhuang, Evaluation of
898 fluorophores for optimal performance in localization-based super-resolution imaging. *Nat*
899 *Methods* **8**, 1027-1036 (2011).
- 900 57. S. Khetan *et al.*, Degradation-mediated cellular traction directs stem cell fate in
901 covalently crosslinked three-dimensional hydrogels. *Nature Materials* **12**, 458-465 (2013).
- 902 58. M. Guvendiren, J. A. Burdick, Stiffening hydrogels to probe short- and long-term cellular
903 responses to dynamic mechanics. *Nat Commun* **3**, 792 (2012).
- 904 59. M. Guvendiren, S. Yang, J. A. Burdick, Swelling-Induced Surface Patterns in Hydrogels
905 with Gradient Crosslinking Density. *Advanced Functional Materials* **19**, 3038-3045 (2009).
- 906 60. G. Lukinavicius *et al.*, Fluorogenic probes for live-cell imaging of the cytoskeleton. *Nat*
907 *Methods* **11**, 731-733 (2014).
908

Table 1

Distance between Fn1-containing nanodomains in fibrils and in non-fibrillar nanodomains

Cell type antibody	Median, nm	Interquartile range, nm	n
Distance between nanodomains in fibrils, nm			
Wild-type MEFs α III ₁₋₆ Fn1 (R184 ab)	148.5	108 – 187	202
Wild-type MEFs monoclonal α Fn1	140	105 – 166	134
Wild-type MEFs polyclonal 297.1	145	107 – 193	159
<u>DOC-treated</u> Wild-type MEFs monoclonal α Fn1	123	83 – 160	148
Fn1 ^{mEGFP/+} monoclonal α Fn1	124	99 – 166	120
Fn1 ^{mEGFP/+} α GFP	115	89 – 155	142
Fn1 ^{mEGFP/+} 4-antibody cocktail	114	82 - 156	106
Distance between non-fibrillar nanodomains, nm			
<u>Non-fibrillar nanodomains</u> Fn1 ^{mEGFP/+} 4-antibody cocktail	329	260 – 410	132

Table 2

Area of Fn1 nanodomains

Cell type antibody	Median $10^{-3} \mu\text{m}^2$	Interquartile range, $10^{-3} \mu\text{m}^2$	n
Area of nanodomains in fibrils, $10^{-3} \mu\text{m}^2$			
Wild-type MEFs α III ₁₋₆ Fn1 (R184 ab)	5	3 – 7	60
Wild-type MEFs monoclonal α Fn1	5	3 – 6	66
Wild-type MEFs polyclonal 297.1	4	3 – 6	62
Fn1 ^{mEGFP/+} monoclonal α Fn1	3	2 – 5	65
Fn1 ^{mEGFP/+} α GFP	4	2 – 6	63
Fn1 ^{mEGFP/+} 4-antibody cocktail	4	3 – 6	62
Area of non-fibrillar nanodomains, $10^{-3} \mu\text{m}^2$			
Untreated Fn1 ^{mEGFP/+} monoclonal α Fn1 16 hr plating	4.3	3– 6	127
11-IIIIC treated Fn1 ^{mEGFP/+} monoclonal α Fn1 16 hr plating	3	2.4 - 4	93
FUD-treated Fn1 ^{mEGFP/+} monoclonal α Fn1 16 hr plating	4	3 – 6	666

Table 3

Number of localizations per Fn1 nanodomain

Cell type antibody	Median	Interquartile range	n
Number of Fn1 localizations per nanodomain within fibrils			
Wild-type MEFs α III ₁₋₆ Fn1 (R184 ab)	72	46.5 - 112	345
Wild-type MEFs monoclonal α Fn1	60	43 – 81	271
Wild-type MEFs polyclonal 297.1	66	42 – 106.5	381
DOC-treated Wild-type MEFs monoclonal α Fn1	72	46 – 113	112
Fn1 ^{mEGFP/+} monoclonal α Fn1	63	45.25 – 114	216
Fn1 ^{mEGFP/+} α GFP	61	39 – 92	351
Fn1 ^{mEGFP/+} 4-antibody cocktail	73	50 – 103	314
Number of Fn1 localizations per non-fibrillar nanodomain			
Fn1 ^{mEGFP/+} 4-antibody cocktail	58.5	39 – 95	62
Untreated Fn1 ^{mEGFP/+} monoclonal α Fn1 Unpermeabilized cells	45	33 – 68	127
11-IIIC treated Fn1 ^{mEGFP/+} monoclonal α Fn1	46	29 – 68.5	93
FUD-treated Fn1 ^{mEGFP/+} monoclonal α Fn1 Unpermeabilized cells	54.5	37 – 92	102

Figure 1

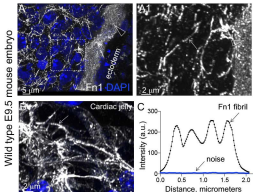


Figure 1. Beaded architecture of Fn1 fibrils in embryonic ECM.

Wild-type E9.5 mouse embryos were fixed and stained with the monoclonal antibody to Fn1 (white) and DAPI, and imaged using 100x oil objective, N.A. 1.49, pinhole 0.8, and sampling rate of 40 nm/pixel. **A – A1.** Sagittal optical section through the first pharyngeal arch and **B.** the cardiac jelly, an ECM-rich region between the myocardial and endocardial layers of the outflow tract of the heart. Large arrowheads in **A – A1** point to the ECM at the ectoderm-mesenchyme boundary of the 1st pharyngeal arch. The box in **(A)** is expanded in **A1** to show Fn1 microarchitecture. Arrow in **A1** points to Fn1 fibril within the arch mesenchyme; **B.** Beaded architecture of Fn1 fibrils in cardiac jelly, e.g., arrow. **C.** Intensity profile plot of a Fn1 fibril shows a regularly-undulating profile, with troughs well above the noise; a.u. arbitrary units.

Figure 2

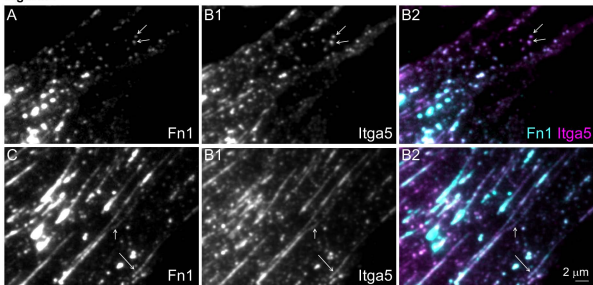


Figure 2. Integrin $\alpha 5$ and Fn1 co-localize in beaded adhesions. Wild-type MEFs were plated for 16 hours on glass coverslips, then fixed, stained with antibodies to Fn1 and integrin $\alpha 5$ (Itga5), and imaged at the critical angle of incidence using 100x oil objective, NA 1.49. **A – A2** cell periphery. Arrows in **A-A2** point at examples of non-fibrillar Fn1 adhesions. **B – B2** medial portion of a cell containing beaded fibrillar adhesions (arrows). Magnifications in all panels are the same.

Figure 3

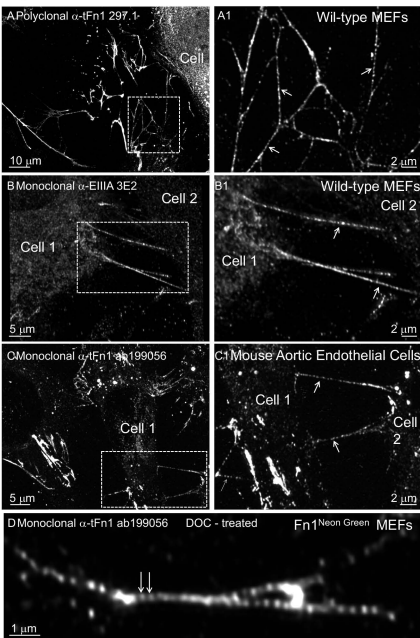


Figure 3. Beaded architecture of Fn1 fibrils is retained in the absence of cell contact. A –B. Fn1 secreted by wild type MEFs and deposited **A)** on glass or **B)** between cells. **C.** Fn1 fibrils between endothelial cells. Boxes in **A – C** are magnified in **A1-C1**. Arrows point to fibrils left behind on substrate (**A1**) or between cells (**B1-C1**). **E.** Fn1 fibril following DOC treatment was imaged using 100x oil objective, NA 1.49, pinhole size 0.8 Airy units, and sampling resolution of 40 nm/pixel in x,y. Note beaded architecture (arrow). Solubilization of cell components is shown in Movie 4.

Figure 4

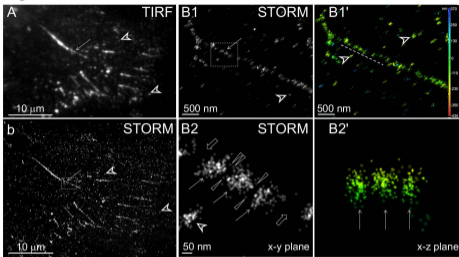


Figure 4. Fn1 fibrils are composed linear arrays of Fn1 nanodomains. $Fn1^{mEGFP/+}$ MEFs were plated on glass for 16 hrs, then fixed and stained with antibodies to GFP followed by secondary antibodies conjugated to Alexa-647. **A.** Native GFP fluorescence imaged by TIRF using 100x objective NA 1.49. Arrow in **a** points to a thin, beaded Fn1 fibril resolved by STORM in **B1** and **B2**. **B.** The entire field of view in **a** is imaged by STORM detecting Alexa-Fluor 647-conjugated antibody (see Methods). The box in **b** is expanded in **B1**. The box in **B1** is expanded in **B2**. The arrow in **B1** points to the same region as the arrow in **A**. Arrows in **B2** point to Fn1 nanodomains; arrowheads point to Fn1 localizations between the nanodomains, notched arrowheads point to Fn1 nanodomains that are not in fibrils, and wide arrows point to Fn1-free areas between the nanodomains in the fibril marked by the arrow in **A**. **A, B, B1, B1'** and **B2** are in x-y planes; **B2'** is in x-z plane. Images in **B1'** and **B2'** are depth-coded according to the scale in **B1'**. See Movie 4 for 3D rotation of the fibril underlined in **B1'** around the x-axis.

Figure 5

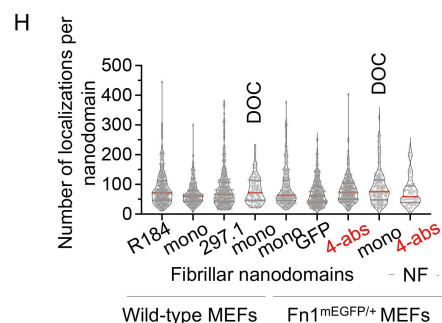
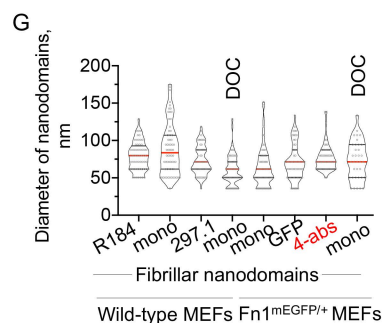
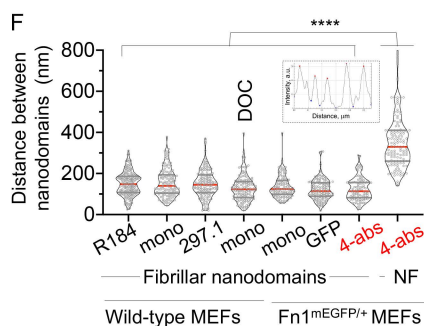
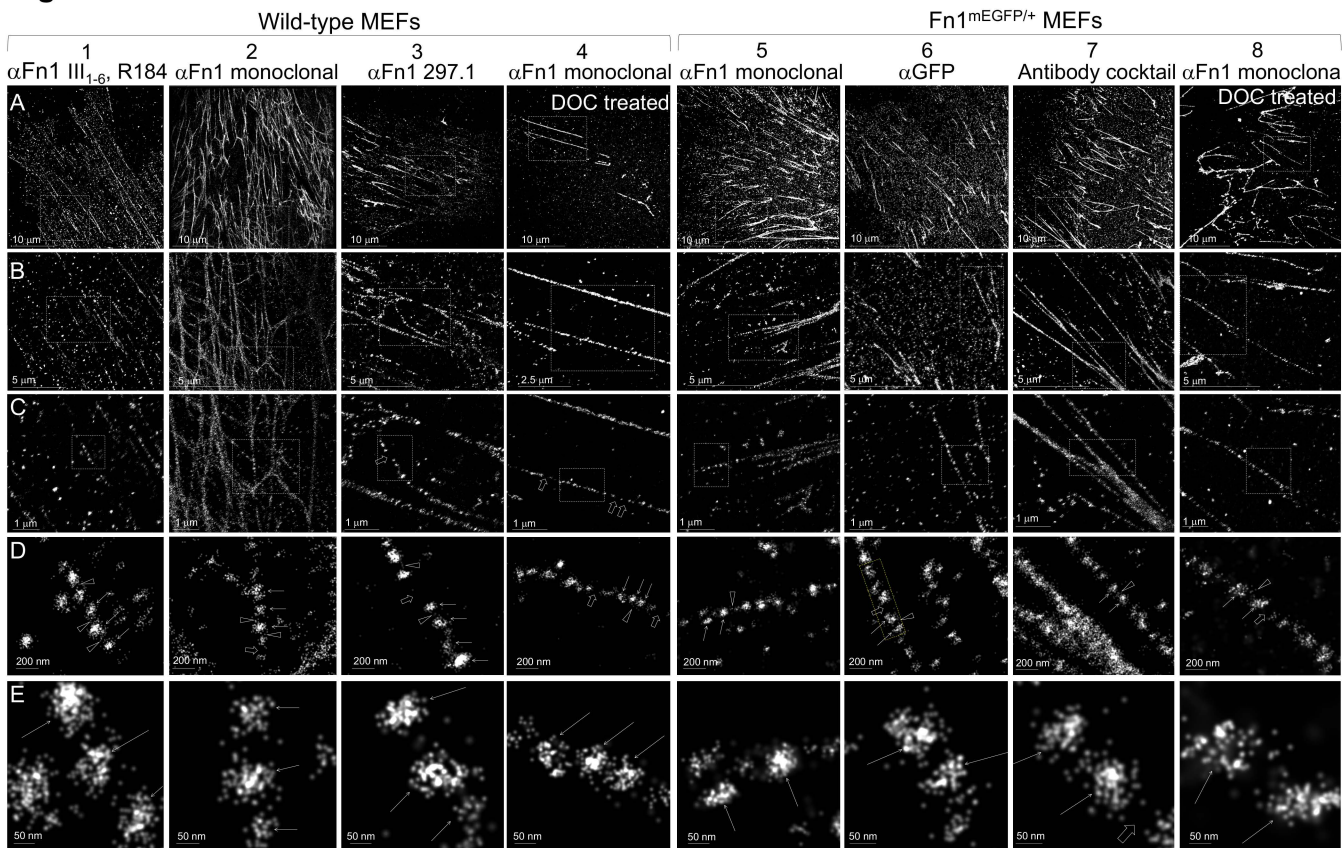
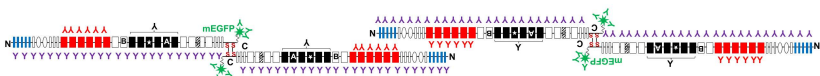
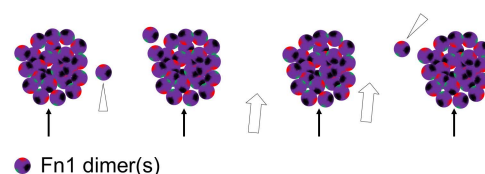


Figure 5. Wild-type or Fn1^{mEGFP/+} MEFs were plated on glass for 16 hrs, fixed and stained with different antibodies to Fn1 followed by Alexa 647-conjugated secondary antibodies. Columns showing cells treated with DOC prior to fixation are marked. Cells were imaged using STORM. **A.** zoom-out views to show the overall appearance of Fn1 fibrils. **B-E.** Successive magnifications of fibrils shown in **(A)**. Arrows in **D** point to nanodomains magnified in **E**; arrowheads in **D-E** point to Fn1 molecules between nanodomains, wide open arrows point to Fn1-free zones between nanodomains in a fibril. **F.** distances between nanodomains within fibrils or non-fibrillar (NF) nanodomains, **** $p < 10^{-4}$, Kruskal-Wallis test, with Dunn's correction for multiple testing. Inset in **F** is a plot profile of the fibril marked by the box in the column **6D** showing regularly-spaced peaks of intensity. DOC-treated samples are marked. 4-antibody cocktail contains four antibodies as in **Model 1**. **G.** Diameter of nanodomains in fibrils. **H.** number of Fn1 localizations per nanodomain in fibrils. **Model 1.** Two Fn1 dimers in a fibril. Depiction of antibody coverage of Fn1 fibrils if dimers were oriented in end-to-end fashion with alternating N- and C-termini. **Model 2.** Our data show that Fn1 fibrils consist of a linear array of nanodomains (black arrows) containing multiple Fn1 dimers (Fn1 dimers are depicted as balls and color-coded according to the antibody scheme in **Model 1**. Arrowheads point to Fn1 and open arrows point to Fn1-free areas between nanodomains.

Model 1 Two Fn1 dimers aligned in a periodical end-to-end fashion. If fibrils were composed of periodically aligned dimers, they would be uniformly stained by the antibody cocktail:



Model 2 Fn1 fibrils form from nanodomains containing multiple Fn1 dimers



■ type I repeat □ type II repeat ▤ type III repeat ▨ V region

● Fn1 dimer(s)

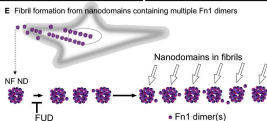
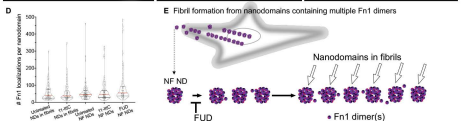
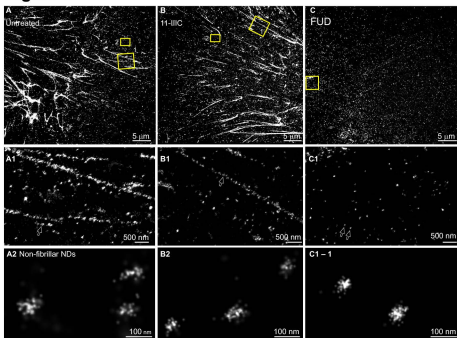
Figure 6

Figure 6. The N-terminal Fn1 assembly domain regulates the organization of Fn1 nanodomains into linear fibrillar arrays. Fn1^{mEGFP/+} MEFs were plated on glass and were either left untreated, or were incubated with the control 11-IIIC peptide, or the FUD peptide for 16 hrs. Cells were then fixed and stained with the monoclonal antibody to Fn1 followed by Alexa 647-conjugated secondary antibodies. Cells were imaged at the critical angle of incidence by STORM. **A – A2.** Untreated, unpermeabilized cells. **B – B2.** Cells incubated with controls 11-IIIC peptide. **C – C1, C1-1** FUD-treated, unpermeabilized cells. Boxes marked 1 in **A-B** were expanded in **A1-B1**. Boxes marked 2 in **A-B**, were expanded in **A2 – B2**. The box in **C** is expanded in **C1** and **C1-1**. Arrows in **A1-B1** point to Fn1 nanodomains (NDs) in fibrils. Arrows in **C1** points to non-fibrillar nanodomains expanded in **C1-1**; **D.** Quantification of the number of Fn1 localizations in NDs in fibrils and in non-fibrillar NDs after various conditions. Red lines mark medians. Differences are not statistically significant, Kruskal-Wallis test with Dunn's correction for multiple testing. **E.** Model of fibril formation: Fn1 dimers assemble into small nanodomains containing integrin $\alpha 5\beta 1$ at cell periphery, move rearward with actin flow, and become organized into linear arrays of nanodomains. Joining of the additional Fn1 nanodomains to these arrays leads to the generation of longer fibrils as the assembly moves toward the cell center. FUD does not interfere with the formation of Fn1 nanodomains. But instead, it blocks the organization of Fn1 nanodomains into linear arrays.